



## **Report**

Course Project: Statistics of Turbulence and the Onset of Chaos

Name: Manon Béchaz

Date: May 20, 2022

Course: Turbulence ME-467

Instructor: Tobias Schneider

# 1 Part I: Statistical Analysis of Turbulence

## 1.1 Introduction

The structure of many turbulent flows encountered in practical situations such as aeronautics, or meteorology is nowadays successfully understood using the Kolmogorov K41 theory. This theory, which is now the most prominent theory of turbulence, covers statistical features of turbulent fluids and gases.

In particular, the latter forecasts a scaling law for the n-th order structure functions, that is moments of velocity increments, which K41 theory claims to be  $S_p(l) = C_p \epsilon^{p/3} l^{p/3}$ , with  $S_p(l) = \langle \delta u_{\parallel}^n(x, l) \rangle$ ,  $\delta u_{\parallel}(x, l)$  the velocity increment,  $\epsilon$  the mean energy dissipation rate per unit mass of the fluid and  $l$  a spatial vector increment. These scaling relations, as well as one of its consequences, namely that the fluid's energy spectrum  $E(k)$  should follow a  $k^{-5/3}$  law (where  $k$  is the wavenumber) are reasonably well supported by experimental and numerical results [1].

Turning to the case of decaying turbulence, the K41 theory predicts that the power law decay observed for the Energy is controlled by large scales. The so-called principle of the permanence of large eddies states that if the turbulent flow is freely decaying, and the energy spectrum is initially self-similar in the infrared range, then this property is preserved for all later times [2]. From this assumption, the theory demonstrates that the decay is slow (power law) and that the small scale scaling  $E \sim k^s$  controls the exponents of the energy decay:  $E \propto (a + t)^{-n}$ , with  $n = (2s + 2)/(3 + s)$ . Eventually, the latter also imposes that the integral scale that defines the inertial range where the K41 theory holds must be time-dependant.

Kolmogorov K41 theory therefore offers a valuable conceptual framework for considering turbulent motions of diverse systems. However, both conceptually and empirically, there are some shortcomings. Specifically, Kolmogorov's K41 theory is for instance based on somewhat questionable hypotheses. Indeed, and mostly based on experimental observations, Kolmogorov assumes a restoration of symmetries in the limit of infinite Reynolds numbers, along with a self-similarity of the turbulent flow at small scales. He also presumes that the energy dissipation rate  $\epsilon$  has a finite non-vanishing limit as the viscosity tends to zero. This last assumption is well supported by experimental and numerical results. The other hypotheses are however more debatable.

Considering first the Reynolds number, the latter inevitably decreases in the case of decaying turbulence as a consequence of the slowdown of the flux. At some point, the K41 theory will therefore fail at describing correctly the physics of the system. Secondly, the central assumption of self-similarity of the random velocity field at inertial-range scales may also well be broken. There is indeed still a doubt about the existence of an intermittency in the inertial range, sometimes experimentally observed in turbulent signals. The latter would invalidate the K41 theory. Eventually, Kolmogorov's theory is based on the assumption of universal scaling coefficients, an hypothesis that can definitely be questioned. As of today, no evidence or disproof of such universal exponents exists.

This work aims at studying turbulence occurring in the Warhaft Wind and Turbulence Tunnel at Cornell University. In particular, we will discuss whether K41 provides an accurate description of the observed data, and to what extend the previous remarks may (or not) impact the predictions of the K41 theory.

## 1.2 Data Analysis

### 1.2.1 Velocity Signal in the Spatial Domain

#### Taylor's frozen flow hypothesis

The velocity signals of the six anemometers is collected in the form of a time series  $u_{tot}(d_i, t)$ .  $x_i$  denotes the position of the anemometer,  $d_i = \{1, 2, 3, 4, 5, 6\}$  m,  $i = \{1, 2, 3, 4, 5, 6\}$ . Under Taylor's frozen flow hypothesis, the latter can however be transformed into a signal of velocity values at different locations, i.e. as a spatial signal. In particular, the hypothesis states that  $u_{tot}(x, t + \tau) \simeq u_{tot}(x - l, t)$ , with  $l = U\tau$  and  $U$  the mean velocity. Note that this hypothesis is correct only in the limit of small velocity fluctuations:

$$I = \frac{\sqrt{\langle \hat{u}^2 \rangle}}{U} \ll 1, \quad (1)$$

with  $\hat{u} = u_{tot} - U$  the velocity fluctuations. This condition will at first be considered valid, and justified and addressed latter in this work.

#### Velocity signal

The obtained streamwise velocities with respect to the upstream distance are presented, for each anemometer, in Figure 1. The same velocities are represented for a smaller range of values of  $x$  in Figure 2. These two figures allow to clearly identify similarities and differences between the datasets.

More precisely, the velocity signals first appear to be both highly disorganized and completely, at least from a statistical point of view, reproducible. As it can be noted in Figure 2, if one look at 2 different time-steps, the obtained velocities are entirely different, and cannot be exactly predicted. This figure also highlights the different structures at all scales: for all anemometers, one perceives structures with distances of the order of 1 m, one-tenth of a m, etc.

However, some properties of the signal seem quite reproducible, and differ from one anemometer to the other. Observing the signal with a larger range as in Figure 1 is in that case more appropriate to observe the similarities and differences. The values of the mean velocities  $U$  and intensities  $I$  provided in Table 1 can also furnish useful insight into the physical situation.

Param.	Dim.	$A_1$	$A_2$	$A_3$	$A_4$	$A_5$	$A_6$
$d$	m	1.0	2.0	3.0	4.0	5.0	6.0
$U$	m/s	10.52	10.52	10.52	10.52	10.52	10.52
$I$	-	0.122	0.055	0.040	0.032	0.027	0.024

Table 1: Mean velocity  $U$  and turbulence intensity  $I$  measured for the 6 anemometers.

One first notices (both on the figure and in the table) that the computed mean velocity is constant whatever the anemometer considered ( $U = 10.52$  m/s), i.e. whatever the distance from the grid. Physically, this is a consequence from the very small fluctuations compared to the mean advection along  $x$ . The mean flow field being incompressible, the mean velocity  $U$  must be constant to ensure continuity.

Secondly, one can observe significant differences in the the spread of the velocity. More precisely, the latter tends to decrease with the distance. This observation is confirmed by the decreasing values of the turbulence intensity in Table 1. Since the turbulence intensity represents the ratio of the spread of the velocity with its mean, if the spread shrink, so does the intensity.

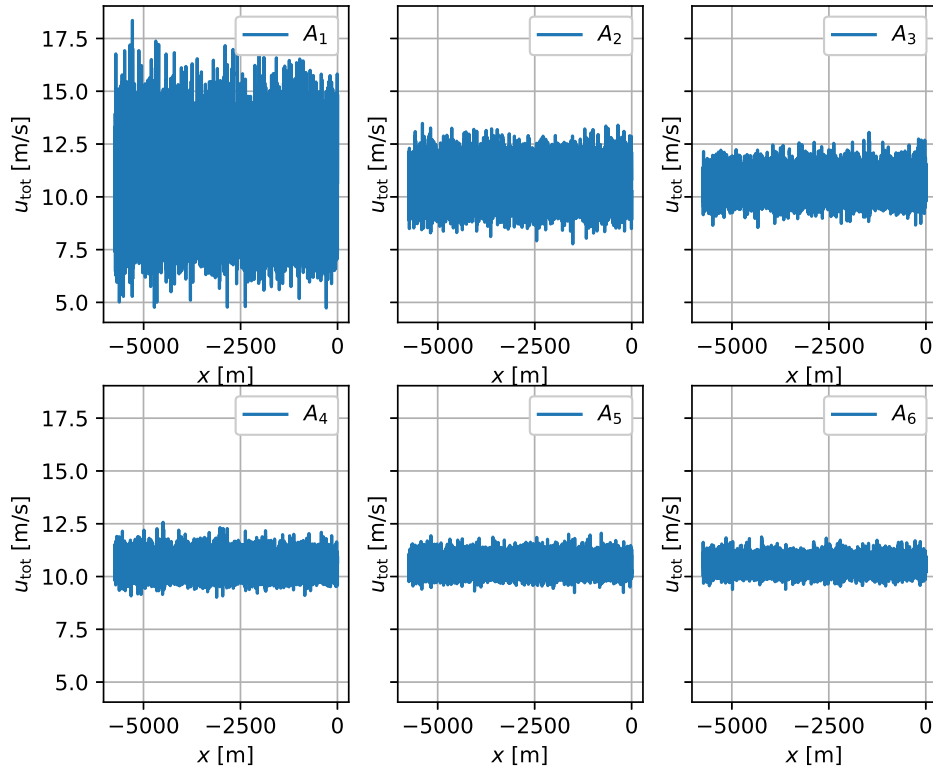
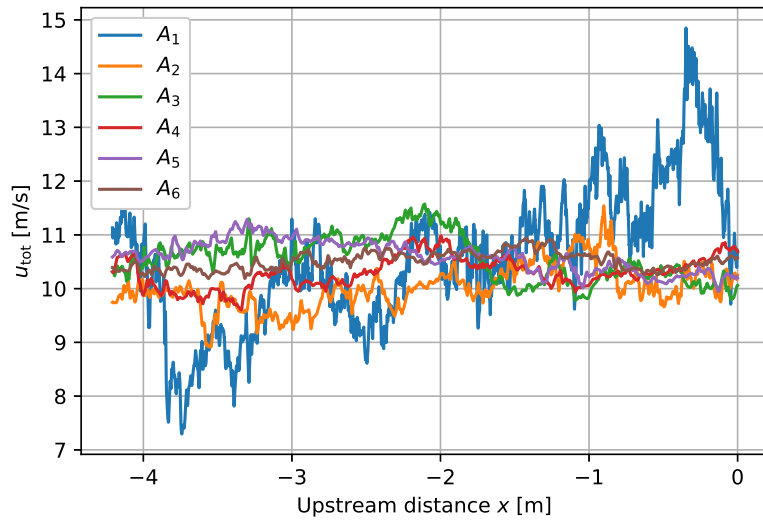


Figure 1: Streamwise velocity signals of the 6 anemometers.

Figure 2: Streamwise velocity signals of the 6 anemometers, for a smaller range of values of the upstream distance  $x$ .

Physically, turbulent eddies create fluctuations in velocity. Because the turbulent motions associated with the eddies are approximately random, we can characterize them using statistical concepts, hence a higher standard deviation indicates a higher level turbulence. Therefore, a diminution of the spread indicates a diminution of the turbulence.

Moreover, this decay of the turbulence intensity with the downstream distance is physically coherent. Indeed, in the absence of mean velocity gradients, the turbulence decays with the distance because there is no production (Note that the energy injection only happens at the grid).

### Verification of the starting hypothesis

Eventually, let's come back to our initial assumption. The hypothesis (1) is satisfied for anemometers 2-6, however one must be careful with the interpretation of the data provided by the first anemometer, whose intensity is higher and might not entirely respect this condition.

#### 1.2.2 Correlation Length of the Velocity Signal

##### Autocorrelation and correlation length

For the velocity fluctuations  $u(x)$ , one defines the autocorrelation as

$$C(l) = \frac{\langle u(x+l)u(x) \rangle}{\langle u^2(x) \rangle}. \quad (2)$$

From the autocorrelation, one further computes the correlation length  $L_c$ , i.e. the length over which the fluctuations are correlated, defined as the length at which  $C(l)$  has dropped to  $1/e$ . Figure 3 presents the value of  $C(l)$  for the six anemometers, along with the associated correlation length  $L_c$ . The precise values of  $L_c$  are reported in table 2.

The values of  $L_c$  augment with the distance to the grid. This is coherent with the previous remarks on the intensity. The latter decreases with the downstream distance, thus indicating a less turbulent flow and therefore a higher correlation length. Indeed, if the flow was not turbulent, it would have been fully reversible and thus fully correlated with previous particle positions, and the correlation length would be very large.

##### Integral scale

The correlation length  $L_c$  approximates the integral scale  $L_{int}$ , given by:

$$L_{int} = \int_0^\infty C(l)dl. \quad (3)$$

$L_{int}$  is numerically integrated using the composite trapezoidal rule. Note that, although it should vanish for large values of  $l$ , strong oscillations of the auto-correlation around zero are observed. In order to avoid incorrect results arising from these oscillations, one integrates until the average, on a window of size  $\Delta l = 1m$ , is zero. After that point, the correlation should, in theory, be zero and therefore not affect the true value of the integral.

The obtained values of  $L_{int}$  are given in Table 2. They are very close to the values of  $L_c$  previously computed. In particular, the error being small, one will use in the rest of this work the correlation length  $L_c$  for the integral scale  $L_{int}$ .

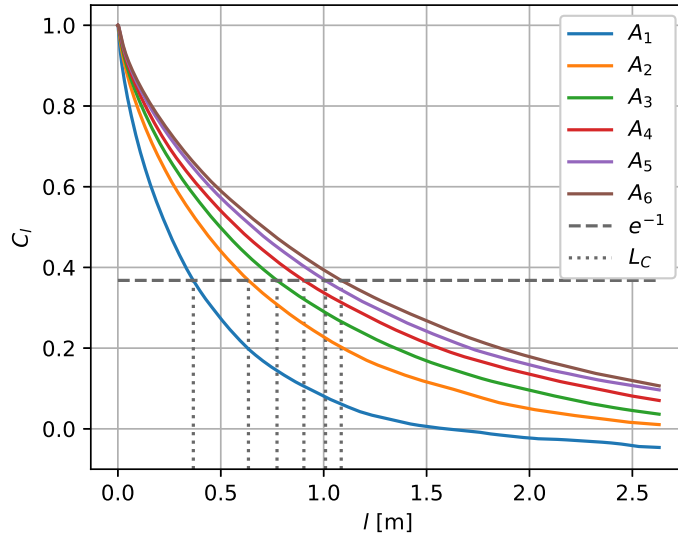


Figure 3: Autocorrelation  $C(l)$  for the six anemometers, and associated correlation lengths  $L_c$ .

Param.	Dim.	$A_1$	$A_2$	$A_3$	$A_4$	$A_5$	$A_6$
$L_C$	m	0.367	0.634	0.773	0.903	1.01	1.09
$L_{int}$	m	0.351	0.623	0.765	0.888	1.00	1.07

Table 2: Correlation length and integral length scale for the 6 anemometers.

### 1.2.3 Energy Spectrum of the Flow

#### Energy spectrum

The goal of this third part is to study the energy spectrum of the flow, defined as  $E(k) = \tilde{E}(k) + \tilde{E}(-k)$ , with  $\tilde{E}$  the density,

$$\tilde{E}(k) = \frac{1}{2} \left| \frac{1}{\sqrt{2\pi L}} \int_0^L u(x) e^{-ikx} dx \right|^2. \quad (4)$$

The energy spectrum is given, for the 6 anemometers, in Figure 4. Note that for the sake of readability, a Savitzky-Golay smoothing filter is applied on the data in order to minimize the noise.

#### Parseval's theorem

As a sanity check to ensure that the normalization is correct, one can make sure that Parseval's theorem is verified:

$$\frac{1}{2} \langle u^2 \rangle = \int_0^\infty E(k) dk. \quad (5)$$

The relative errors between the left hand side and the right hand side of the previous equation are reported, for each anemometer, in Table 3. The relative error, ranging from 1% to 10%, remains relatively small, while still being non negligible. It could however be decreased, for instance by augmenting the number of point used for the integration (500 have been used here). Nevertheless, the conducted study is enough to ensure a correct normalization.

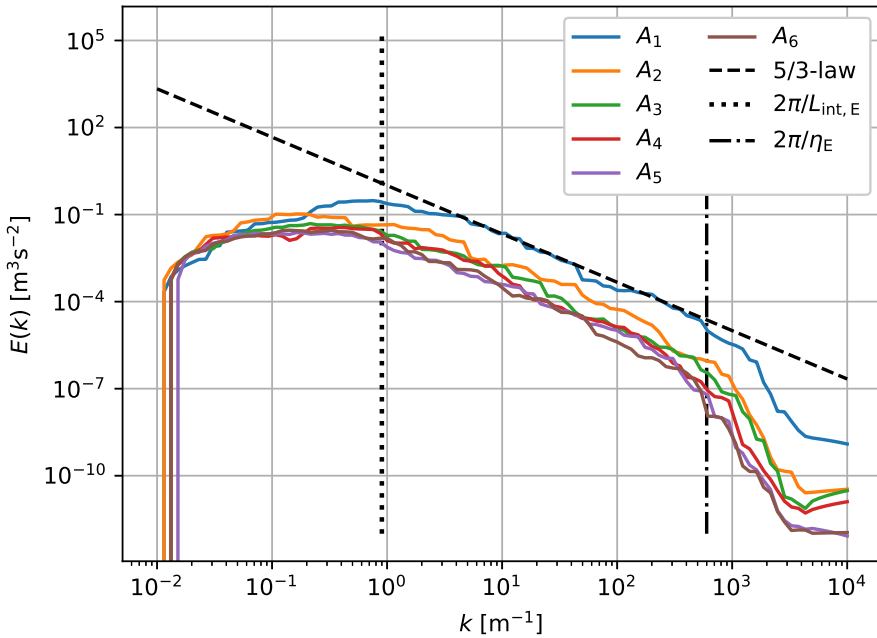


Figure 4: Energy spectra for all 6 anemometers, and estimated wavenumbers corresponding to the integral scale  $L_{\text{int},E}$  and the Kolmogorov scale  $\eta_E$ .

Param.	$A_1$	$A_2$	$A_3$	$A_4$	$A_5$	$A_6$
Relative error [%]	9.8	1.6	12	7.5	1.7	7.0

Table 3: Relative error between the computed RHS and LHS of equation (5).

### Predictions of the K41 theory

According to K41, in the inertial range, the Energy spectrum  $E(k)$  is proportional to  $k^{-5/3}$ , more precisely  $E(k) \propto \epsilon^{2/3} k^{-5/3}$ , with  $k$  the wave number and  $\epsilon$  the energy dissipation rate. The spectrum in Figure 4 is consistent with this theory:

- In the center of the wavenumber range, all the spectra exhibit powerlaw behavior with  $p = -\frac{5}{3}$  as predicted by K41. In this range, there is no injection or dissipation of energy, this is the so called inertial range.
- At high wavenumber, i.e. small length scales, the energy is dissipated and the spectra decay more rapidly than a powerlaw.
- At low wavenumber, i.e. large length scales, one has energy injection that leads to an increase of the energy spectrum.

The three regions described above are separated by the integral scale  $L_{\text{int},E}$  and the Kolmogorov scale  $\eta_E$ . The latter are reported in Table 4. Note that the length scales have been determined graphically, resulting in a low accuracy. In particular, although one could have expected differences in  $L_{\text{int},E}$  and  $\eta_E$  as in table 2, no difference between the six anemometers is visible to the naked eye.

Param.	Dim.	$A_1$	$A_2$	$A_3$	$A_4$	$A_5$	$A_6$
$L_{\text{int},E}$	m				7		
$\eta_E$	m				$1 \cdot 10^{-2}$		

Table 4: Integral and Kolmogorov length scales obtained from the energy spectra.

### 1.2.4 The Dissipation Rate and Different Reynolds Numbers

#### Estimation of the energy dissipation rate $\epsilon$

The energy dissipation rate  $\epsilon$  can be estimated from the velocity fluctuations at the integral scale where energy is injected into the energy cascade:

$$\epsilon = \frac{1}{2} \frac{\sqrt{\langle u^2 \rangle^3}}{L_C}. \quad (6)$$

The value obtained for each downstream probe distance is provided in Table 5. One notices that the energy dissipation rate is much larger for the first anemometer as is for the following. Generally, the dissipation rate declines with probes' downstream position,  $d$ , and losses 2 order of magnitude between the data obtained for the first and the last anemometer. This clear diminution is once again linked to the weakening of the turbulence intensity, or equivalently to the spread of the velocity signal, as proved by equation (6). The more intense the turbulence are, the quicker the dissipation is and the larger the rate. Hence the results are coherent with the intensities obtained in table 1.

#### Taylor Reynolds number and Outer-scale Reynolds number

It is traditional in turbulence theory to not use the Reynolds number based on the integral scale,  $Re$ , but instead the so-called Taylor-scale Reynolds number  $Re_\lambda$ . The two Reynolds number are defined as:

$$Re = \frac{L_C U}{\nu} \quad \text{and} \quad Re_\lambda = \frac{\lambda \sqrt{\langle u^2 \rangle}}{\nu}, \quad (7)$$

with  $\lambda = \sqrt{\frac{15\nu\langle u^2 \rangle}{\epsilon}}$  the Taylor length scale. When the Reynolds number is high, the Taylor-scale Reynolds number is related to the integral-scale Reynolds number by

$$Re_\lambda \sim Re^{1/2}. \quad (8)$$

The estimations of the two Reynolds number for each downstream probe are given in Table 5. A few comments can be made on the results. First, one observes inverse trends for  $Re$  and  $Re_\lambda$ : when  $Re$  increases,  $Re_\lambda$  decreases.  $Re$  is moreover very large, thus verifying one of the hypothesis of the K41 theory, that is that  $Re$  must tend to  $\infty$ . Note eventually that the ratio between  $Re_\lambda^2$  and  $Re$  is approximately constant as expected from equation (8).

Param.	Dim.	$A_1$	$A_2$	$A_3$	$A_4$	$A_5$	$A_6$
$\epsilon$	$\text{m}^2 \text{s}^{-3}$	2.87	$1.51 \cdot 10^{-1}$	$4.66 \cdot 10^{-2}$	$2.11 \cdot 10^{-2}$	$1.15 \cdot 10^{-2}$	$7.49 \cdot 10^{-3}$
$Re_\lambda$	-	973	858	805	783	762	744
$Re$	-	259308	448655	546780	639166	713577	767452
$Re_\lambda^2/Re$	-	3.65	1.64	1.19	0.96	0.81	0.72

Table 5: Dissipation rate and Reynolds numbers for all 6 anemometers.

### 1.2.5 Turbulence Decay

In a wind tunnel, turbulence decays as it moves downstream from the grid. The goal of this part is to examine the predictions of the law of decay of turbulence for the experimental setup used here.

#### Kinetic energy

The overall kinetic energy per unit mass of the flow is :

$$\varepsilon = \frac{3}{2} \langle u^2 \rangle. \quad (9)$$

Indeed, the kinetic energy is defined to be half the sum of the variances of the velocity components:

$$\varepsilon = \frac{1}{2} (\langle u_x^2 \rangle + \langle u_y^2 \rangle + \langle u_z^2 \rangle). \quad (10)$$

Using the isotropic property of the turbulences, one has  $\langle u_x^2 \rangle = \langle u_y^2 \rangle = \langle u_z^2 \rangle = \langle u^2 \rangle$ , hence the first expression of the kinetic energy per unit mass of the flow.

The values of the overall kinetic energy per unit mass of the flow are given in table 6.

Param.	Dim.	$A_1$	$A_2$	$A_3$	$A_4$	$A_5$	$A_6$
$\varepsilon$	$\text{m}^2\text{s}^{-2}$	2.46	0.499	0.260	0.170	0.122	0.096

Table 6: Overall kinetic energy for all 6 anemometers.

#### Scaling of the kinetic energy

The theory of turbulence decays predicts that the kinetic energy should scale as:

$$\varepsilon \propto (d - d_0)^{2h/(1-h)}, \quad (11)$$

where  $d_0$  is the position of the so-called virtual spatial origin, and  $h$  is the scaling exponent of the large-scale scaling,  $u_l \sim Cl^h$ . From the values of  $\varepsilon$ , one can thus deduce the values of  $d_0$  and  $h$ . Three methods have been used here.

#### Method 1: Numerical fitting

The first method relies on appropriate numerical fitting using python's function `curve_fitting`. Obtained values for  $d_0$  and  $h$  are reported in Table 7 (*Method 1*).

#### Method 2: Graphical approach

Taking the logarithm of equation (11), one gets:

$$\log(\varepsilon) = \frac{2h}{1-h} \log(d - d_0). \quad (12)$$

Hence, for the correct value of  $d_0$ , the log-log plot of  $\varepsilon$  wrt.  $(d - d_0)$  should follow a straight line, with slope  $\frac{2h}{1-h}$ .

A second method to determine  $d_0$  and  $h$  is thus to plot the logarithm of  $\varepsilon$  wrt. the logarithm of  $(d - d_0)$  for a wide range of values for  $d_0$ . Using python's function `polyfit`, one can then compute for each value of  $d_0$  the linear regression of  $\log(\varepsilon)$  wrt.  $\log(d - d_0)$ . `polyfit` allows to obtain both the value of the

slope,  $q = \frac{2h}{1-h}$ , and the value of the residual of the fit. Eventually, the best value of  $d_0$  is the one that minimizes the residual (because it means that the plot is linear in a log-log scale). The value of  $h$  is obtained from the corresponding optimal value of  $q$ . The obtained values are given in table 7 (*Method 2*).

Figure 5 present the plot of the logarithm of  $\varepsilon$  wrt. the logarithm of  $(d - d_0)$ , for different values of  $d_0$  as described in the previous paragraph. Note that many more values have been tested (100 in total), but have not been represented on the figure for the sake of readability. The dashed line correspond do the the optimal value of  $q$ , it is clearly aligned with the plot for  $d_0 = 0.640$  that is the corresponding optimal value obtained.

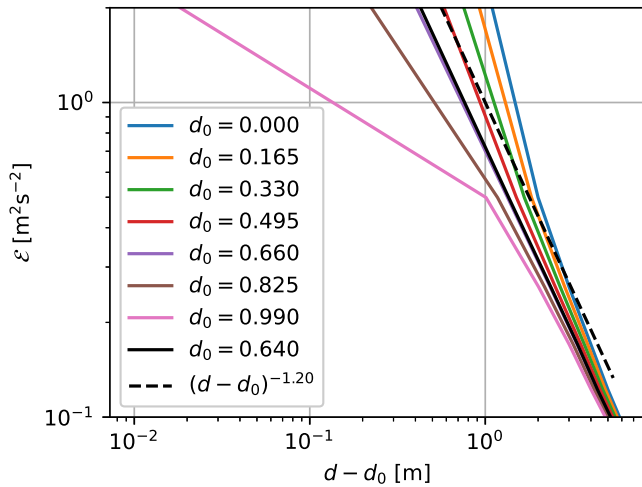


Figure 5: Overall kinetic energy per unit mass with respect to  $d - d_0$  for different values of  $d_0$ .

### Method 3: Theoretical predictions

Using that the integral scale  $l_0$  scales as  $l_0 \sim (d - d_0)^{1/(1-h)}$ , it can easily be shown from equation (11) that the kinetic energy content of the flow,  $\varepsilon$ , scales with the integral length scale,  $l_0$ , as:

$$\varepsilon \propto l_0^{2h}. \quad (13)$$

As before, this implies that the log-log plot of  $\varepsilon$  wrt.  $l_0$  should follow a straight line, with slope  $2h$ . The log-log plot of  $\varepsilon$  wrt.  $l_0$  is provided in Figure 6, along with theoretical predictions:

- $2h = -3$  (Saffman's decay),
- $2h = -5$  (Loitsyanskii's decay),
- $2h = -2$  (self-similar decay).

Clearly,  $2h = -3$  appears to be the best decay scenario. More precisely, if one uses `polyfit` to compute the slope of the curve, one gets  $2h = 2.98$  which is very close to Saffman's decay scenario.

Assuming that  $2h = -3$ , one can determine  $d_0$  using the same fitting methodology as for the second Method. Equation (11) indicates that the plot of  $\varepsilon$  wrt  $(d - d_0)^{q_{th}}$ , with  $q_{th} = \frac{2h_{th}}{1-h_{th}}$  and  $h_{th} = -1.5$  should follow a straight line. Computing with `polyfit` the linear regression of  $\varepsilon$  wrt.  $(d - d_0)^{q_{th}}$  for different values of  $d_0$ , and minimizing the residual, one determines the value of  $d_0$ . Similar to what was previously for the second method, the plots used for the estimation of  $d_0$  are provided in figure 7. The obtained value is given in Table 7 (*Method 3*).

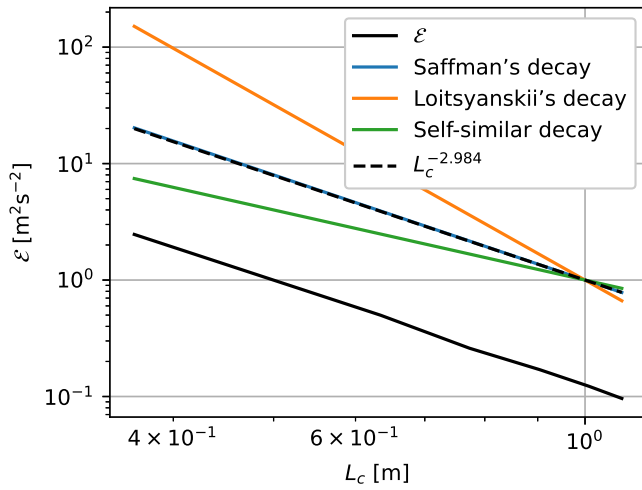


Figure 6: Overall kinetic energy per unit mass with respect to the correlation length  $L_c$ , along with different theoretical predictions.

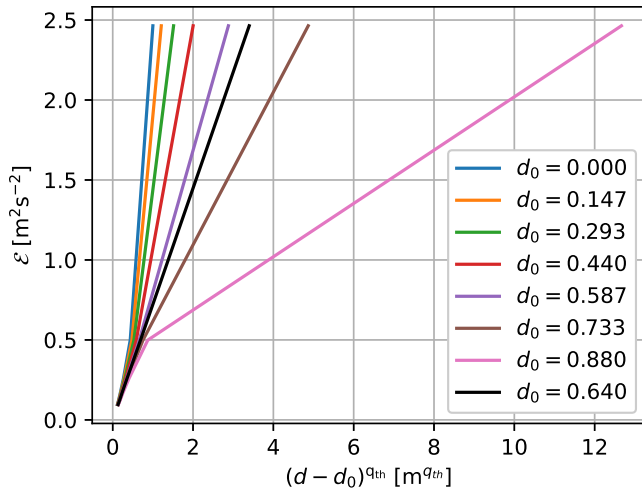


Figure 7: Overall kinetic energy per unit mass with respect to  $(d - d_0)^{q\text{-th}}$  for different values of  $d_0$ .

Param.	Dim.	Method 1	Method 2	Method 3
$d_0$	m	0.643	0.640	0.640
$h$	-	-1.48	-1.50	-1.49

Table 7: Fitting parameters from decay theory obtained from the 3 methods.

### Comparison of the three Methods

Looking at the different methods and at the obtained values, several remarks can be made. First, one notices that the three methods give almost identical results.

From a numerical point of view, the first method is by far the easiest one. However, this method is highly sensitive to noise, especially with the limited number of datapoints at our disposal for the fitting. We encounter the same negative points for the second method, where the only difference is the fitting method. Note that if we had not used `polyfit`, and only determined the best fit visually, the results

would have been a lot less accurate.

This problem of sensitivity to noise is solved with the third method, that faces other issues. The latter allows to link our results to theoretical ones, however it is limited because it only consider 3 values for  $h$ . If the obtained value does not match any of the 3 values, the method is, at least partially, useless. One can in that case still compute the value of  $2h$  using a linear fit, but one cannot link it to a theory.

### Energy spectrum

Assuming that the velocity has infrared asymptotic self-similarity with exponent  $h < 0$ , i.e.  $u_l \sim Cl^h$ , the principle of permanence of large eddies, expressed in the Fourier domain, implies that

$$E(k) \sim k^{-(2h+1)}. \quad (14)$$

The experimental energy spectrum, along with the theoretical prediction (Equation (14)) are presented in Figure 8, for wavelengths  $k$  way smaller than the integral scale. Theoretical prediction fits surprisingly well with experimental results, thus validating the principle of permanence of large eddies. This principle states that if the turbulent flow is freely decaying, and initially possesses the property of infrared asymptotic self-similarity with a scaling exponent  $-5/2 < h < 0$  and a constant  $C$ , then this property is preserved for all later times with the same constant. Here, the fact that the slope of the Energy spectrum is constant independently of the downstream distance, i.e. independently of the time is a perfect illustration of the principle.

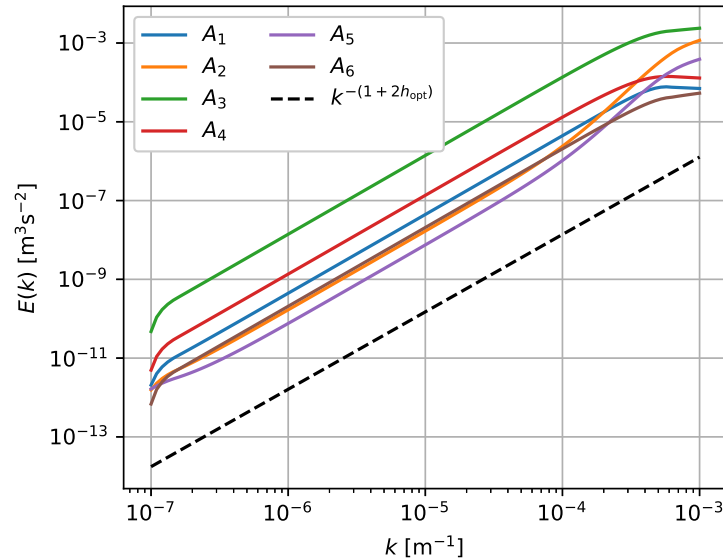


Figure 8: Energy spectra of all 6 anemometers in the infrared range of wavenumbers, along with theoretical predictions obtained from equation (14).

### Interpretation of $d_0$

$d_0$  is not called the virtual origin for nothing. In particular, it can be interpreted as the origin point of the turbulence. In our case, the virtual origin is located after the grid, at  $d_0 = 0.64$  m. This means that the turbulence do not start right after the grid, but need some time to fully develop.

Many scaling relation exist that link the virtual origin  $d_0$  to different physical quantities. From a theoretical point of view, all these scaling relation are equivalent and should therefore provide identical estimation of  $d_0$ .

### 1.2.6 Velocity Increments

#### Longitudinal velocity increment and differences between length scales

For the dataset acquired at a downstream distance  $d_1 = 1\text{m}$ , Figure 9 presents the longitudinal velocity increment  $\delta u_{||} = u(x + l) - u(x)$  for  $l = \{1\text{mm}, 1\text{cm}, 10\text{cm}, 10\text{m}\}$ . The first value of  $l$  is smaller than  $\eta_E$ , estimated in section 1.2.3 at 1cm, i.e. exactly the value of the second value of  $l$ . The third one lies in the inertial range, while the last one is just above the upper limit of the inertial range,  $L_{\text{int,E}} \approx 7\text{ m}$ .

One notices that the longitudinal velocity increments behaves differently depending on the scale considered. The mean value remains constant at 0, however its spread (i.e. its variance) increases with the scale.

All these observations are coherent with the previous remarks. The variance is small for small values of  $l$ , showing that the velocities' values are close, hence correlated. On the other hand, the variance is high for large values of  $l$ , implying that the velocities of two points separated by a large distance  $l$  might be significantly different: the two velocities are not correlated.

#### Flatness of the velocity increment signal

For each  $l$ , the probability distribution of  $\delta u_{||}$  has a bell-shaped curve. To investigate how close such a curve is to the Gaussian distribution, one compares the flatness of the velocity increment signal, with that of the Gaussian distribution, given by:

$$f(l) = \frac{\langle \delta u_{||}(x, l)^4 \rangle}{\langle \delta u_{||}(x, l)^2 \rangle^2} \quad (15)$$

$$= \frac{3\sigma^4}{(\sigma^2)^2} \quad (16)$$

$$= 3. \quad (17)$$

Figure 10 presents the flatness of the velocity increment signal, along with that of a Gaussian distribution. For large values of  $l$ , the flatness of the velocity increment signal converges to 3, i.e. to the flatness of the Gaussian distribution. Hence, for large values of  $l$ , the probability distribution  $\delta u_{||}$  can be well approximated by a Gaussian distribution. For small values of  $l$  however, the flatness increases.

This observation is problematic. As a matter of fact, K41 predicts the scaling  $S_n(l) \sim l^{n/3}$  for the structure functions in the inertial range, thus yielding for the flatness:

$$f(l) = \frac{\langle \delta v_{||}(l)^4 \rangle}{\langle \delta v_{||}(l)^2 \rangle^2} \sim \frac{l^{4/3}}{(l^{2/3})^2} \sim 1. \quad (18)$$

Putting it another way, the flatness should be constant in the inertial range. The increasing flatness noticed when  $l$  decreases thus indicates a deviation from the K41 theory. In fact, flatness is usually used to quantify intermittency, i.e. to measure how much Kolmogorov's K41 theory deviates from experimental measurements [3]. A higher flatness implies a larger probability of outliers of the velocity increments at scale  $l$ , hence the name of intermittency at small scales. The scaling  $S_n(l) \sim l^{n/3}$  being

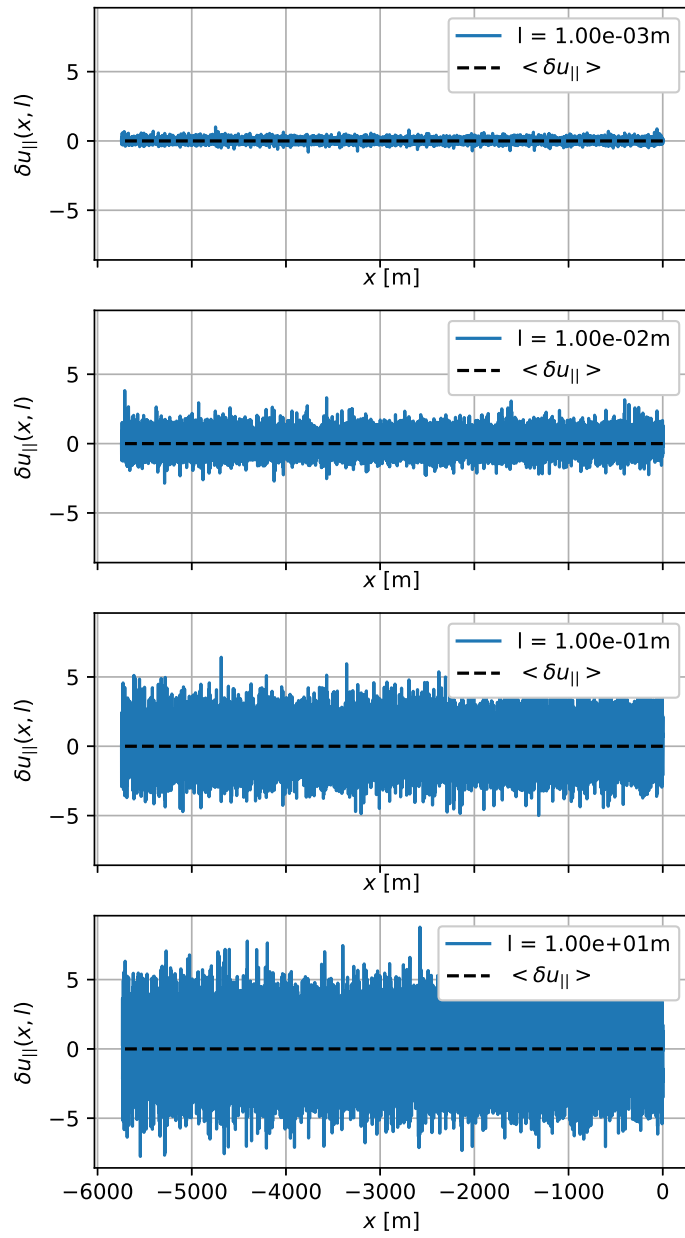


Figure 9: Velocity increments for different values of  $l$  and for the first anemometer.

derived from the self-similar scaling hypothesis, the observations made in Figure 10 point out a violation of this hypothesis.

### 1.2.7 Structure Functions and Energy Dissipation

The structure function of the velocity field is a very valuable tool for analyzing turbulence. The latter is defined as

$$S_n(l) = \langle \delta u_{||}^n(x, l) \rangle. \quad (19)$$

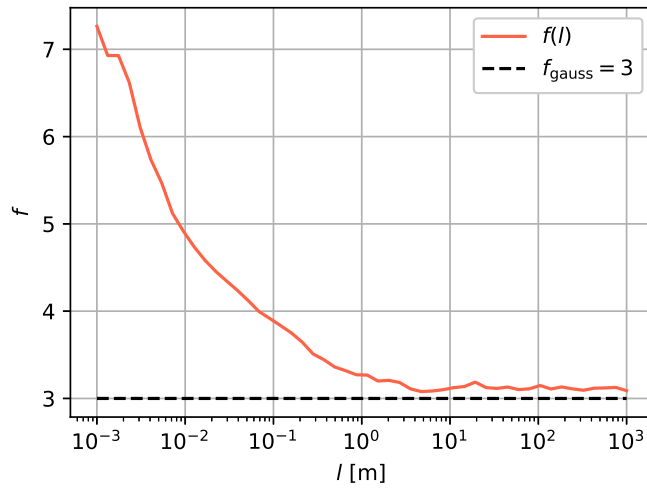


Figure 10: Flatness  $f$  against  $l$  for the first anemometer.

### Second order structure function

K41 predicts the following scaling of  $S_2(l)$ :

$$S_2(l) \propto \epsilon^{2/3} l^{2/3} \quad (20)$$

Moreover, the Wiener formula implies that when the energy spectrum is a power-law

$$E(k) \propto k^{-n}, \quad 1 < n < 3, \quad (21)$$

then the second order spatial structure function is also a power-law:

$$S_2(l) \propto l^{n-1}. \quad (22)$$

This relation between the two scalings make the link between the two-thirds law (20) and the Kolmogorov energy spectrum:

$$E(k) \propto \epsilon^{2/3} k^{-5/3}. \quad (23)$$

Figure 11a present the second order structure function for the dataset acquired at distance  $d_1 = 1\text{m}$ . The theoretical scaling  $l^{2/3}$  is also represented, which allows to estimate the range over which the  $2/3$  law is correct. It also enable the comparison with the range over which the scaling of the Kolmogorov energy spectrum is valid (i.e. the inertial range, whose bounds are  $\eta_E$  and  $L_{\text{int},E}$  provided in Table 4). The two ranges, given in Table 8, are of the same order of magnitude.

	2/3-law for $S_2(l)$	5/3-law for $E(k)$
Range of validity of $k$ [m]	$1 \cdot 10^{-2} - 1$	$1 \cdot 10^{-2} - 7$

Table 8: Ranges of validity of the  $2/3$ -law for  $S_2(l)$  and the  $5/3$ -law for  $E(k)$

### Third order structure function

Turning to the third order structure function, and according to K41, the latter should follow the four-fifth law:

$$S_3(l) = -\frac{4}{5}\epsilon l. \quad (24)$$

As previously, Figure 11b presents the third order structure function for the dataset acquired at distance  $d_1 = 1\text{m}$ , along with the theoretical predictions arising from the four-fifth law. Once again, we see that the 4/5 law is respected, for values of  $l$  ranging from  $10^{-3}$  to  $5 \cdot 10^{-1}$ .

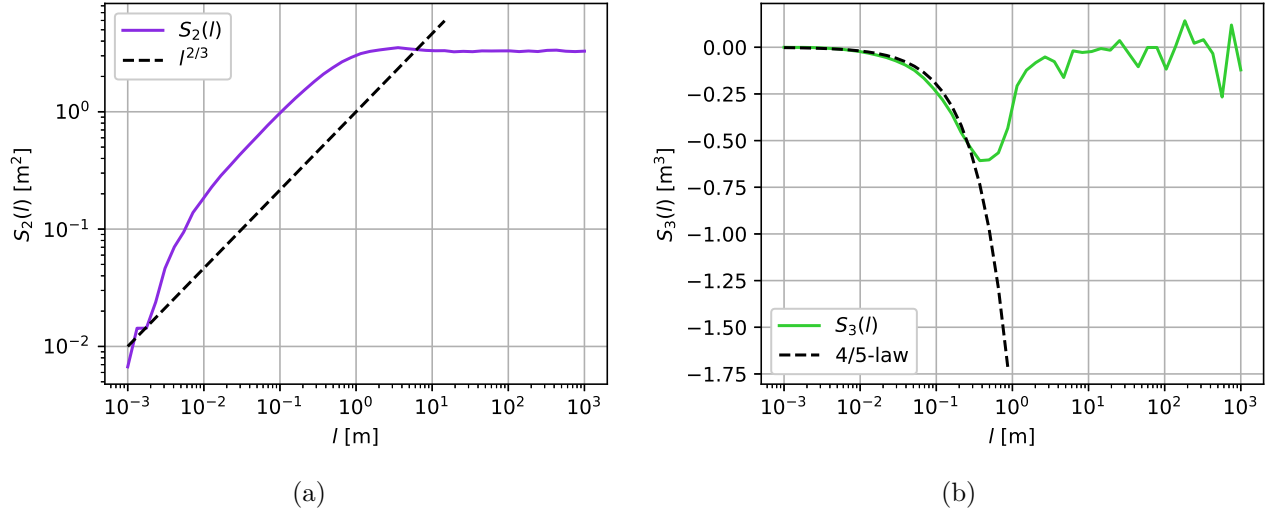


Figure 11: (a) Second and (b) third-order structure functions, and associated scaling relations (2/3-law and the 4/5-law).

### Estimation of the energy dissipation rate $\epsilon$

Eventually, one can estimate the value of  $\epsilon$  from the second and third order structure functions. Using that  $S_2(l) = C_2 \epsilon^{2/3} l^{2/3}$ , with  $C_2 \approx 2.2$  and  $S_3(l) = -\frac{4}{5}\epsilon l$ , one gets:

$$\epsilon = \frac{1}{l} \left( \frac{S_2(l)}{C_2} \right)^{3/2} = -\frac{5}{4} \frac{S_3(l)}{l}. \quad (25)$$

Both estimations of  $\epsilon$  are shown in Figure 12, with the value determined in section 1.2.4 indicated as a reference. In the inertial range, one can note that both estimation are approximately constant and close to value obtained from the integral scale. Taking the mean value, in the inertial range, of the obtained values of  $\epsilon$  can thus yield a first estimation of the dissipation rate (Method a). We could however also retrieve the value of  $\epsilon$  from a direct curve fit (Using python's method `curve_fit`) on  $S_2(l)$  and  $S_3(l)$  (Method b). This second method may lead to more accurate results. The estimations of  $\epsilon$  obtained from the two approaches, as well as the reference value estimated from the integral scale in section 1.2.4, are reported in Table 9. For both methods, the results are really close to the reference value.

Method	Integral scale	Method a	Method b
$\epsilon$ obtained from $S_2$ [m <sup>2</sup> s <sup>-3</sup> ]	2.87	2.71	2.93
$\epsilon$ obtained from $S_3$ [m <sup>2</sup> s <sup>-3</sup> ]		2.67	3.02

Table 9: Values of the energy dissipation rate  $\epsilon$  obtained with different methods.

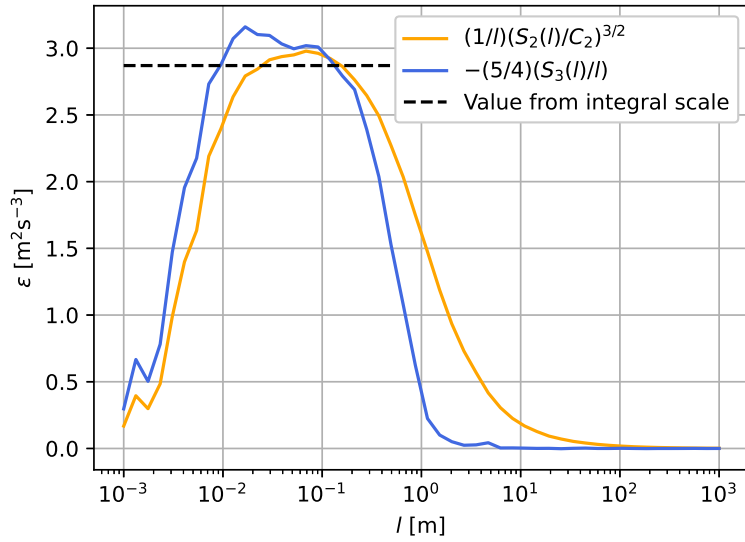


Figure 12: Energy dissipation rate  $\epsilon$  obtained from the second and third order structure functions, along with the reference values deduced from the integral scale.

### 1.3 Discussion

The initial objective of this study was to assess whether the K41 theory was providing an accurate description of the observed data or not. In this regard the results are mixed and not fully conclusive.

On one hand, the results are consistent with the theory on many points. Looking at the energy spectrum, the latter exhibits as predicted from the K41 theory a power law behavior with exponent  $p = -5/3$ , and allows to determine (although in an approximate way) an inertial range where the K41 theory holds. Turning to the structure functions, the K41 scaling relations can also be retrieved, with similar ranges of validity. The observed differences can probably be attributed to the low precision of their graphical estimation. On the other hand, the observation of a non constant flatness of the velocity increments tend to prove the invalidity of the self-similarity hypothesis and the probable incorrectness of the K41 theory.

These deviations from the K41 theory can be caused both by the non-ideal experimental setup and by features of turbulence that the K41 theory fails to describe properly. From an experimental point of view, several aspects can be noted. First, the whole study relies on the Taylor hypothesis that allows to transform the measured time series onto a spatial signal. The underlying hypothesis is correct only in the limit of small velocity fluctuations, limit that has been proven in section 1.2.1 to be more or less verified, therefore being a plausible source of errors. Secondly, in an ideal turbulence experiment, the Reynolds number would be infinite, which is in practice impossible and can be a second possible source of mistakes.

From a theoretical point of view, and as underlined in the introduction, there is still a doubt about the existence of an intermittency in the inertial range. The latter could in particular explain the increase of the flatness observed in section 1.2.6. This lack of self-similarity could invalidate the K41 theory and thus explain the observed discrepancies.

Concerning the decay scenario, finding the law of decay is still an open problem. On that point, our study underlines different and sometimes contradictory results. The main goal is to estimate the value

of the parameter  $h$ , that controls the power law decay of the Energy. When  $h > -1$ , the outer Reynolds number increases, leading to a non trivial asymptotics for large times. This is the behavior that could be expected from the growing values of  $Re$  computed in section 1.2.4. The values of  $h$  obtained in section 1.2.5 however indicate the inverse trend. In particular, the three methods used provide approximately the same value for  $h$ , namely  $h = -1.5$ . The latter is not only numerically accurate (the numerical fit is indeed very good), but is also analytically consistent with Safmann's decay theory. This decay law therefore seems, in view of our data, the most plausible. The increasing Reynolds number could be a consequence from a poor approximation of the integral scale with the correlation length, and hence not contradict Safmann's decay theory. Regardless of the decay theory and the value of  $h$ , one has however a clear power law decay of the Energy, as predicted by K41.

To conclude, this work has been confronted to the usual inconsistencies of the K41 theory. While being mostly verified throughout the study, some discrepancies of the K41 with respect to the observation have been noticed. This work also suggested Safmann's theory as the most plausible decay scenario.

## 2 Part II: Nonlinear Dynamics and the Emergence of Chaos

### 2.1 Introduction

Analysis of turbulence is closely linked to the chaos phenomenon of sensitive dependence on initial conditions. Having a deep understanding of the non linear dynamics and the emergence of chaos is therefore essential to fully explain the phenomena behind the emergence of turbulence.

To this end, this second part aims at analysing the dynamics of the Baker's map, amongst others its attractors, their dimension, and Lyapunov exponents. The generalized Baker's map is indeed a great example to study how chaos emerges in deterministic systems. Simply put, this map involves compressing the unit square, stretching it, cutting vertically the resulting rectangle and stacking the resulting pieces.

### 2.2 Analysis of the Dynamics

#### 2.2.1 Implementation of the Map and (Numerical) Observations

##### Implementation of the Baker's map

The map is defined, in the unit square  $[0, 1] \times [0, 1]$  as follows:

$$\begin{aligned} x_{n+1} &= \begin{cases} \alpha_1 x_n & \text{if } y_n < \beta \\ (1 - \alpha_2) + \alpha_2 x_n & \text{if } y_n \geq \beta \end{cases} \\ y_{n+1} &= \begin{cases} y_n / \beta & \text{if } y_n < \beta \\ (y_n - \beta) / (1 - \beta) & \text{if } y_n \geq \beta \end{cases}, \end{aligned} \quad (26)$$

where  $\alpha_1$ ,  $\alpha_2$  and  $\beta$  are real valued parameters verifying  $\alpha_1 + \alpha_2 \leq 1$  and  $0 < \beta < 1/2$ .

The repeated application of the Baker's map to points colored red and blue, initially separated depending on the value of  $y_0$  is presented in Figure 13. The first iteration consists of two strips of width  $\alpha_1$  and  $\alpha_2$  respectively, that got flattened, stretched, cut and stacked to yield the second iteration. The latter is composed of 4 strips, 1 of width  $\alpha_1^2$ , 2 of width  $\alpha_1\alpha_2$ , and 1 of width  $\alpha_2^2$ . The 4 strips fit inside the corresponding strip on the previous step. The procedure is pursued to the the number of iterations required. After several iterations, the red and blue points seem to be completely mixed.

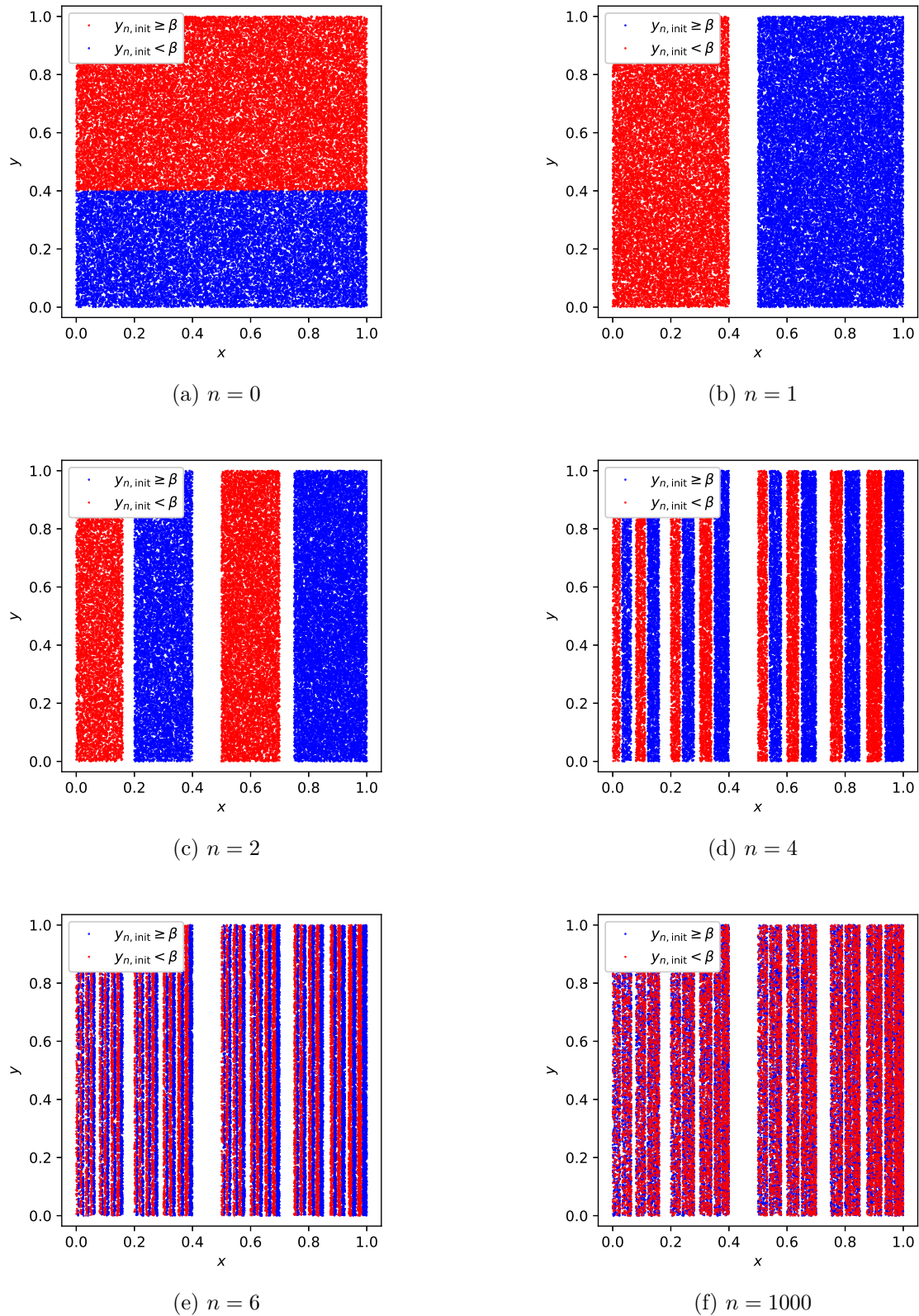
All in all, at each iteration, the obtained figure consists of  $2^n$  strips with width determined by the values of  $\alpha_1$  and  $\alpha_2$ , separated by empty areas. The successive images of the square are nested in each others. The map is moreover not area preserving. Indeed, one notices on Figure 13 that each application of the map shrinks the volume. Since the map does not preserve area, it allows for the existence of attractors, and a consequence of this diminution of the volume is that the orbit must converge eventually onto something that has no area. In particular, if one denotes by  $B^n(S)$  the set of points obtained after applying  $n$  times the Baker's map on the initial set  $S$ , one has the following inclusion relation:

$$B^{n+1}(S) \subset B^n. \quad (27)$$

When  $n \rightarrow \infty$ , the limiting set  $\Lambda$  is thus:

$$\Lambda = \bigcap B^n(S). \quad (28)$$

Note that by Cantor's intersection theorem,  $\Lambda$  is not empty, it has however measure zero.

Figure 13: Baker's Map evolution for 50000 points,  $\alpha_1 = 0.4$ ,  $\alpha_2 = 0.5$  and  $\beta = 0.4$ .

### Influence of the parameters $\alpha_1$ and $\alpha_2$

As previously underlined, the values of  $\alpha_1$  and  $\alpha_2$  control the width of the strips as well as the width of the gaps. Indeed, at each iteration, the total number of bands is  $2^n$ , with width distributed as follow: for  $k = 1, 2, \dots, n$ , one has  $\binom{n}{k}$  bands of width  $\alpha_1^k \alpha_2^{n-k}$ . The total width of the bands is

$$B = \sum_{k=0}^n \binom{n}{k} \alpha_1^k \alpha_2^{n-k} = (\alpha_1 + \alpha_2)^n, \quad (29)$$

thus yielding a total width of the gaps  $G = 1 - (\alpha_1 + \alpha_2)^n$ . If  $\alpha_1 + \alpha_2$  was equal to 1, there would not be any gaps.

Figure 14 present the system after 6 iterations, for different values of  $\alpha_1$  and  $\alpha_2$ . As expected, small values of  $\alpha$ 's yield large gaps, and vice versa. For  $\alpha_1 = \alpha_2 = 0.5$ , there is no gap as anticipated.

### Emergence of chaos

Stretching and folding is characteristic of topological characterisation of chaos. As a result, one would expect the Baker's map to display some chaotic behavior. As a matter of fact, the Baker's map exhibits extreme sensitive dependence on initial conditions. In particular, two points initially close together will be sent far apart after a some iterations. This property is illustrated in Figures 15 and 16. In the two examples presented in these figures, the two pink points, initially separated by only  $10^{-4}$ , are after 1000 applications very far apart. This highlights the sensitivity to initial conditions, characteristic of the emergence of chaos in a system.

Despite this chaotic behavior, one notes the presence of an attractor  $\Lambda$ , as derived at the beginning of this section. As a matter of fact, one notices on Figure 13, 15 and 16 that the repartition of the points tend to the same pattern after 1000 iteration. This limiting set is self similar, composed of the same initial separation in two strips (as in Figure 13 for  $n = 1$ ), repeated over and over in each strip.

#### 2.2.2 Strange Attractor and Fractal Dimensions

##### Box counting dimension of the attractor

As noticed before, the attractor  $\Lambda$  is self similar and can be characterized by a fractal dimension. We will use the so-called box counting dimension to compute it. Intuitively, this distance counts the number of boxes of length  $r$  necessary to cover a topological object. It is defined as:

$$D_0 = \lim_{n \rightarrow \infty} \frac{\log(N(r))}{\log(1/r)}, \quad (30)$$

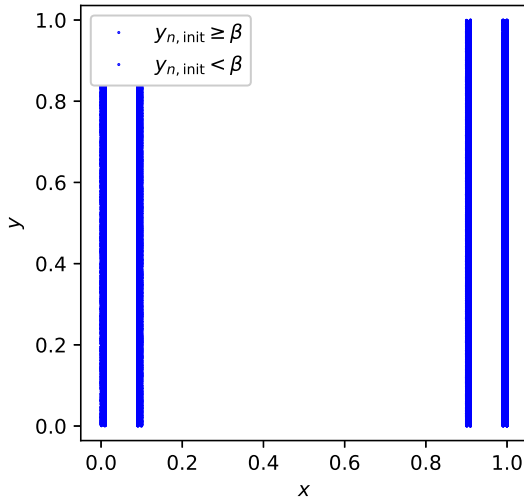
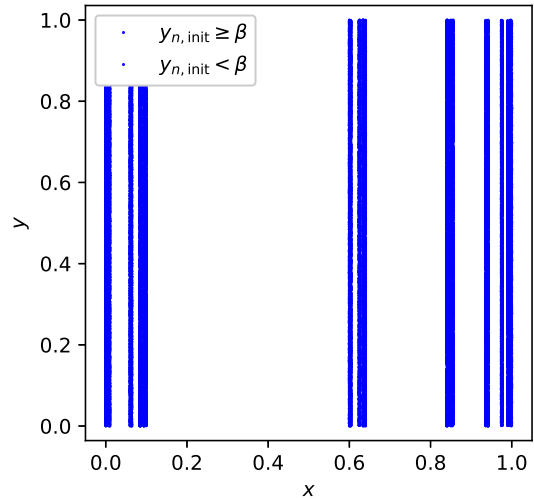
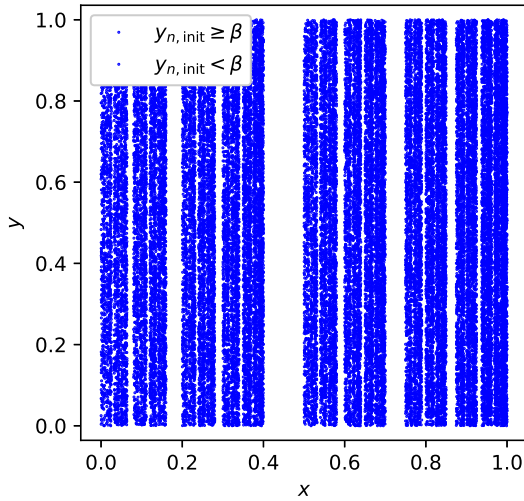
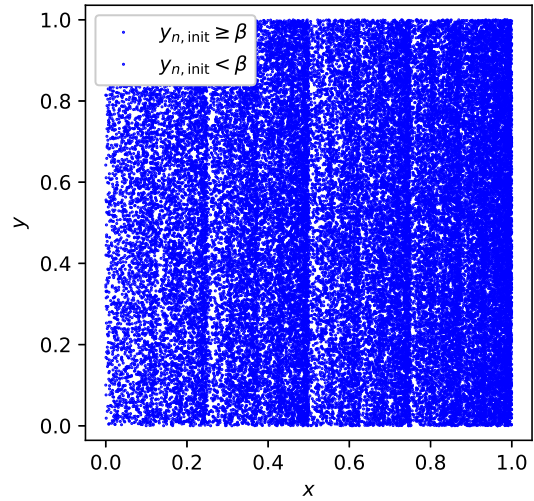
with  $N(r)$  the number of occupied boxes,  $r$  the side length of a box and  $n$  the iteration.

Let's consider the case  $\alpha_1 = \alpha_2 = \alpha$  and the  $n$ -th iteration. All the points in the system are grouped in  $2^n$  bands of width  $\alpha^n$ . One will therefore use boxes of side length  $r = \alpha^n$ . Each strip has length 1, and can thus be covered by  $\frac{1}{\alpha^n} = \alpha^{-n}$  boxes. The total number of boxes is:

$$N_n = 2^n \alpha^{-n} = \left(\frac{\alpha}{2}\right)^{-n}. \quad (31)$$

Consequently, the box counting distance is :

$$D_0 = \lim_{n \rightarrow \infty} \frac{\log(N_n)}{\log(1/r)} = \lim_{n \rightarrow \infty} \frac{\log((\alpha/2)^{-n})}{\log(\alpha^{-n})} = 1 + \frac{\log(1/2)}{\log(\alpha)}. \quad (32)$$

(a)  $\alpha_1 = \alpha_2 = 0.1$ (b)  $\alpha_1 = 0.1, \alpha_2 = 0.4$ (c)  $\alpha_1 = 0.4, \alpha_2 = 0.5$ (d)  $\alpha_1 = \alpha_2 = 0.5$ Figure 14: Baker's Map after 6 iterations, for 50000 points and different values of  $\alpha_1$  and  $\alpha_2$ , and  $\beta = 0.4$ .

For  $0 < \alpha < 1/2$ ,  $D_0$  is between 0 and 1 as expected. Indeed, if  $n \rightarrow \infty$ , one is left with a bunch of lines that almost fill an area, hence the dimension between 1 (dimension of a line) and 2 (dimension of an area). Similarly,  $D_0 \rightarrow 2$  as  $\alpha \rightarrow 1/2$ , which also make sense with our previous observations since the volume is conserved (the total width of the gaps is zero) and the system fills the whole space, which is in 2 dimensions.

### Numerical estimation of the box counting dimension of the attractor

Numerically, the box counting dimension can be estimated from the system obtained after a large number of iterations. In this case, the limiting set is approximated by the set of point obtained after

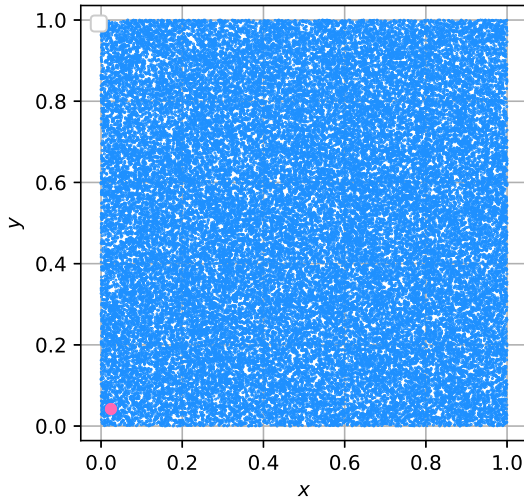
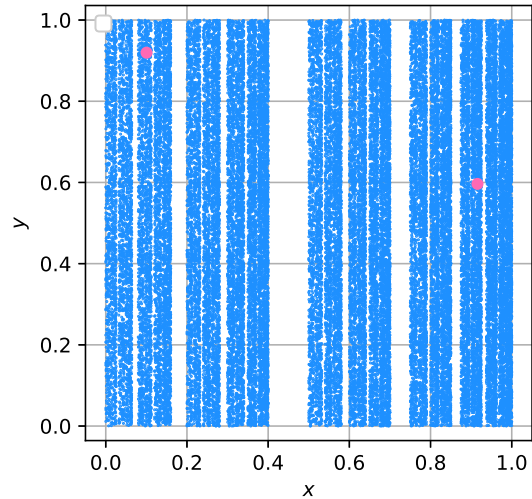
(a)  $n = 0$ (b)  $n = 1000$ 

Figure 15: Evolution of 2 initially close points after 1000 iterations.

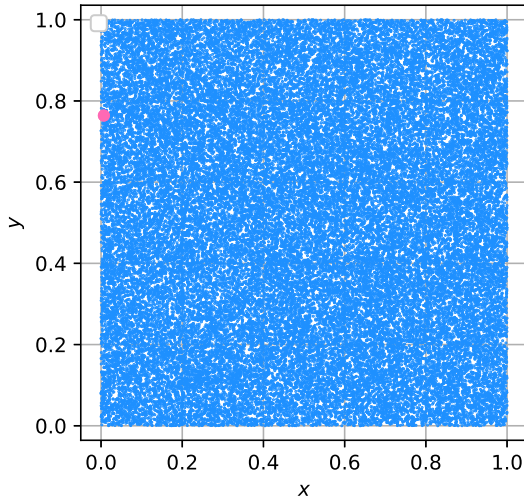
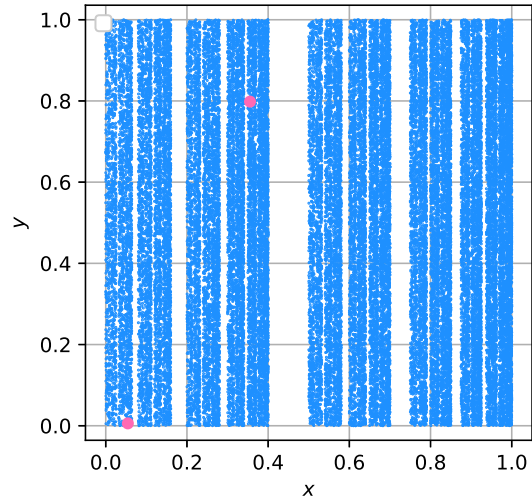
(a)  $n = 0$ (b)  $n = 1000$ 

Figure 16: Evolution of 2 initially close points after 1000 iterations.

2000 iterations, and 50000 points are simulated. For different values of  $r$ , the number  $N(r)$  of occupied boxes of size  $r \times r$  is deduced from the 2d-histogram of the points by counting the non-zero bins. Equation (30) indicates a linear relationship between  $\log(N(r))$  and  $\log(1/r)$ , with slope  $D_0$ . Hence, by computing the corresponding linear regression, one eventually gets an estimate for the value of  $D_0$ . The values obtained for  $\alpha \in \{0.1, 0.2, 0.3, 0.4, 0.5\}$  are reported in Table 10.

The estimated numerical values are somewhat close to the analytical values, with errors of less than 10%. It is however surprising that we arrive at such close values. Indeed, if we represent  $\log(N(r))/\log(1/r)$  as a function of  $1/r$ , we should, according to equation (30), have a constant value. However, as seen in

Figure 17, this far from being the case. For a number of boxes larger than  $10^2$ , the latter undeniably decrease, and even for smaller values the curves are not constant. Empirically, one deduces that the range of number of boxes used for the fitting and the calculation of  $D_0$  should not exceed  $10^2$ . Note that the values in table 10 have been obtained with  $1/r \in [10^0, 10^2]$ .

These results highlight potential issues of the method. On one hand, one should have a consequent number of boxes such that we are in the limit  $r \rightarrow 0$ . On the other hand however, if the boxes are too small, we will end up with incorrect empty boxes, that result from the finite number of points simulated. The latter are at the origin of the decrease of  $\log(N(r))/\log(1/r)$  for  $1/r$  greater than  $10^2$  observed in Figure 17.

Looking at the result themselves, one notices as expected that the dimension augments with the value of  $\alpha$ . Indeed, when  $\alpha$  increases, the total width covered by the strips augments as well, hence a higher dimension. Eventually, for  $\alpha = 0.5$ , the computed dimension is 2, as previously anticipated and discussed.

$\alpha$	Analytical value	Numerical value	Relative difference [%]
0.1	1.30	1.37	5.59
0.2	1.43	1.55	8.16
0.3	1.58	1.72	9.31
0.4	1.76	1.88	6.77
0.5	2.00	2.00	0.08

Table 10: Numerical and analytical values of the box counting dimension  $D_0$ , for different values of  $\alpha_1 = \alpha_2 = \alpha$ .

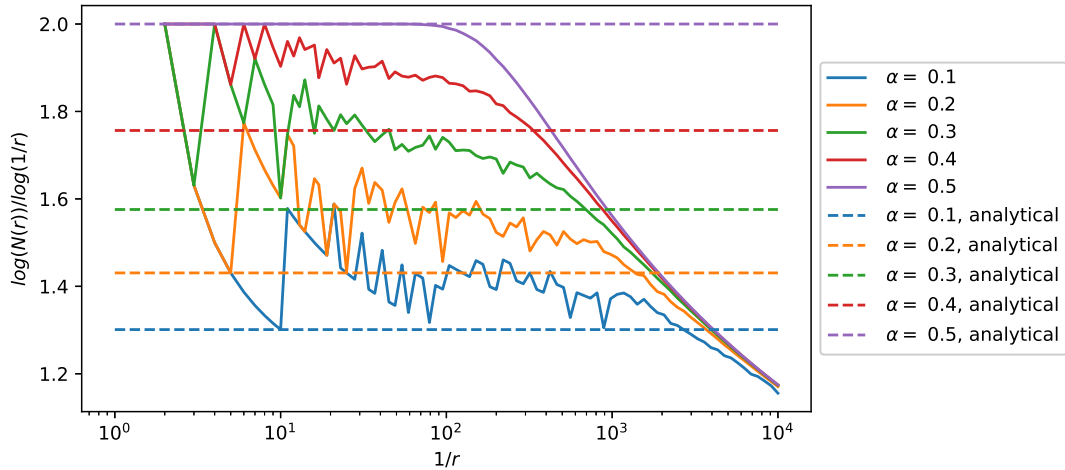


Figure 17: Evolution of the Minkowski distance  $D_0$  with respect to the number of boxes, for different values of  $\alpha_1 = \alpha_2 = \alpha$ .

### 2.2.3 Chaos and Lyapunov Exponents

#### Analytical computation

Turning to the Lyapunov exponents, the latter are defined as follows:

$$\lambda = \lim_{n \rightarrow \infty} \lim_{|\epsilon_0| \rightarrow 0} \frac{1}{n} \sum_{j=0}^n \log(|J(x_j, y_j)\hat{\epsilon}_0|), \quad (33)$$

with  $\epsilon_0 \in \mathbb{R}^2$  a small perturbation of the initial condition,  $\hat{\epsilon}_0 = \epsilon_0/|\epsilon_0|$  and  $J$  the Jacobian of the map.

One will consider the case  $\alpha_1 = \alpha_2$  and  $\beta = 1/2$ . The definition of the Baker's map (equation (26)) can be cast into the following matrix form:

$$\begin{cases} \begin{pmatrix} x_{n+1} \\ y_{n+1} \end{pmatrix} = \begin{pmatrix} \alpha & 0 \\ 0 & 2 \end{pmatrix} \begin{pmatrix} x_n \\ y_n \end{pmatrix} & \text{if } y_n < 1/2 \\ \begin{pmatrix} x_{n+1} \\ y_{n+1} \end{pmatrix} = \begin{pmatrix} \alpha & 0 \\ 0 & 2 \end{pmatrix} \begin{pmatrix} x_n \\ y_n \end{pmatrix} + \begin{pmatrix} 1-\alpha \\ -1 \end{pmatrix} & \text{if } y_n \geq 1/2 \end{cases} \quad (34)$$

In both cases, the Jacobian matrix of the application is

$$J = \begin{pmatrix} \alpha & 0 \\ 0 & 2 \end{pmatrix}. \quad (35)$$

The Jacobian is diagonal, its eigenvalues are  $\mu_1 = \alpha$  and  $\mu_2 = 2$ , thus implying the following Lyapunov exponents:

$$\lambda_1 = \log \alpha, \quad (36)$$

$$\lambda_2 = \log 2. \quad (37)$$

## Numerical computation

Numerically, the first Lyapunov exponent can be obtained by recalling that it can be expressed as:

$$\lambda_1 = \lim_{n \rightarrow \infty} \lim_{|\epsilon_0| \rightarrow 0} \frac{1}{n} \log \frac{|\epsilon(n)|}{|\epsilon_0|}, \quad (38)$$

with  $\epsilon(n)$  the separation vector between two trajectories initially perturbed by  $\epsilon_0$ . Hence, by computing the difference between two initially close points at successive time steps  $n$ , one can deduce via a linear fit between  $\log |\epsilon(n)|/|\epsilon_0|$  and  $n$  the value of  $\lambda_1$ .

The estimation of the second Lyapunov exponent is more complex and requires a prior assumption. Its estimation is based on the approximation of the Jacobian by finite differences. Supposing that the eigenvectors of  $J$  are the  $x$  and  $y$  directions, one computes the sum in equation 33 for a finite number  $n$  of iterations.

The results obtained for various values of  $\alpha$  is provided in Table 11, along with the corresponding analytical values. The numerical results fit the analytical values extremely well, which was expected from the trivial form of the Jacobian (which is for instance diagonal as assumed).

## Lyapunov exponents and noteworthy properties of the map

The values of the Lyapunov exponents allow deduce some properties of the Baker's map.

First, one notices that the first Lyapunov exponent is negative since  $\alpha < 1$ , while the second,  $\log 2$ , is positive. The trajectories of two initially close points evolving like  $\epsilon(t) = \epsilon_0 e^{-\lambda_i t}$ , this implies that the map tend to compress the set in the  $x$  direction, and to expand the separation in the  $y$ -coordinate. Once again, the results are coherent with the previous observations, where we observed that two points initially close where quickly separated, and were we also underlined the diminution of the size of the bands along the  $x$ -axis.

$\alpha$	$\lambda_1$ An. value	$\lambda_1$ Num. value	$\lambda_1$ Rel. diff. [%]	$\lambda_2$ An. value	$\lambda_2$ Num. value	$\lambda_2$ Rel. diff. [%]
0.1	-2.303	-2.303	0.00	0.693	0.693	0.01
0.2	-1.609	-1.609	0.00	0.693	0.693	0.04
0.3	-1.204	-1.204	0.00	0.693	0.693	0.09
0.4	-0.916	-0.916	0.00	0.693	0.692	0.16
0.5	-0.693	-0.693	0.00	0.693	0.691	0.25

Table 11: Analytical and numerical values of the Lyapunov exponents, for different values of  $\alpha_1 = \alpha_2 = \alpha$ .

As a second graphical observation, we note that  $\lambda_1 + \lambda_2 = 0$  only for  $\alpha = 0.5$ , meaning that the system is conservative, i.e. preserves the volume of the phase space, only in the case  $\alpha_1 = \alpha_2 = 0.5$ . We retrieve the results observed in Figure ?? where the volume is preserved (no gaps are observed) only in the case  $\alpha_1 = \alpha_2 = 0.5$ .

### 2.3 Discussion

The study of the Baker's map has allowed to understand some key features and properties of chaos and to assess the possibility of studying them numerically.

First, we observed how chaos can emerge from, at first sight, simple equations. Similarly, chaos can arise from non-linearity in the Navier-Stokes equation at high Reynolds numbers. Such easy equations can lead to very complex trajectories, sensitive to initial conditions. However, one can still derive some useful properties. In our case, the computation of the Lyapunov exponents have enabled to characterize the long term divergence of infinitesimally close trajectories. The Baker's Map's fractal character was further underlined with the numerical estimation of the fractal dimension.

Direct application of these methods can be obtained by replacing the dynamical evolution of vorticity, as described by Euler's equation, by the action of discrete maps [4]. As a matter of fact, the property of self-similarity characteristic for fractal elements is also assumed in the K41 theory for the velocity increments, and the fractal dimension is essential to K41 theory. Eventually, the conservative property of the Baker's map for  $\alpha_1 = \alpha_2 = 0.5$  can be linked to the supposed space-filling of the eddies. Studying the non conservative case  $\alpha_1 + \alpha_2 \neq 0.5$  can thus help understanding the corrections to K41 arising from intermittency.

## Link to GitHub repository

<https://github.com/mannexbcz/Turbulences>

## References

- [1] Mohd Yaacob, Rasmus Schlander, Preben Buchhave, and Clara Velte. Experimental evaluation of kolmogorov's-5/3 and 2/3 power laws in the developing turbulent round jet. *Journal of Advanced Research in Fluid Mechanics and Thermal Sciences*, 45:14–21, 05 2018.
- [2] Uriel Frisch. *Turbulence: The Legacy of A. N. Kolmogorov*. Cambridge University Press, 1995.
- [3] Daniel Eceizabarrena and Victor Vilaça Da Rocha. An analytical study of flatness and intermittency through riemann's non-differentiable functions, 2021.
- [4] Stephen Childress. Turbulent baker's maps. *SIAM Journal on Applied Mathematics*, 55(2):552–563, 1995.

## List of Collaborators

- Arthur CORNET
- Philipp WEDER

## Personal Statement

I hereby certify that I fully respect the stated Honor Code and specifically that:

1. My report is my original work prepared solely by me;
2. All sources used are cited;
3. All people I collaborated with are listed.

---

Signature (Manon Béchaz)

---

Date